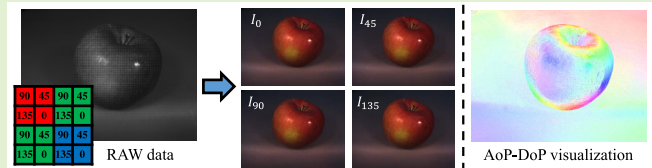


Monochrome and Color Polarization Demosaicking Based on Intensity-Guided Residual Interpolation

Miki Morimatsu, Yusuke Monno¹, Member, IEEE, Masayuki Tanaka¹, Member, IEEE, and Masatoshi Okutomi¹, Member, IEEE

Abstract—A division-of-focal-plane or microgrid image polarimeter enables us to acquire a set of polarization images in one shot. Since the polarimeter consists of an image sensor equipped with a monochrome or color polarization filter array (MPFA or CPFA), the demosaicking process to interpolate missing pixel values plays a crucial role in obtaining high-quality polarization images. In this study, we proposed a novel MPFA demosaicking method based on intensity-guided residual interpolation (IGRI) and extended it to CPFA demosaicking. The key of IGRI is generating an effective intensity guide image, for which we proposed two methods considering four-directional intensity and polarization edge information. We also constructed a new full color-polarization image dataset captured using a 3-CCD RGB camera and a rotating polarizer. By using the constructed dataset, we experimentally validated that our IGRI-based methods outperform existing methods in MPFA and CPFA demosaicking.

Index Terms—Division-of-focal-plane polarimeter, microgrid polarimeter, polarization filter array, color-polarization image dataset, demosaicking.



I. INTRODUCTION

POLARIZATION is a physical property of an electromagnetic wave such as light consisting of perpendicularly oscillating electric and magnetic fields [1]. Many studies have shown that polarization parameters, such as the angle of polarization (AoP) and the degree of polarization (DoP), are valuable for various image processing and computer vision applications, such as specular removal [2], reflection separation [3], and 3D shape reconstruction [4], [5].

Polarization images refer to a set of images acquired with different polarizer angles, from which polarization parameters are calculated for every pixel. Polarization images are typically captured by sequentially rotating a linear polarizer placed in front of a camera [6]. However, this conventional approach is not suitable for dynamic scenes and video acquisition, since it requires multiple shots for capturing a set of images.

As another approach, a division-of-focal-plane or microgrid image polarimeter acquires polarization images by

using an image sensor equipped with a polarization filter array (PFA) [7]. A typical monochrome PFA (MPFA) consists of a 2×2 periodical pattern of four polarizers with the angles of 0, 45, 90, and 135 degrees, respectively. Similarly, an image sensor equipped with the so-called quad-Bayer color PFA (CPFA) is recently produced with a much-reduced price from existing color-polarization sensors [8]. These PFA-based sensors are suitable for dynamic scenes and video capturing, since they enable the one-shot acquisition of monochrome or color polarization pixel values. For the PFA-based sensors, the demosaicking, which is an interpolation process of missing polarization pixel values, is a key component in acquiring high-quality polarization images.

Many demosaicking methods have been proposed for MPFA, including interpolation-based [9]–[19] (see [7] for a survey), dictionary-learning-based [20], [21], and deep-learning-based [22]–[24] methods. A few methods have also been proposed for CPFA based on reconstruction-based [25], [26], dictionary-learning-based [27] and deep-learning-based [28] approaches. Although deep-learning-based methods have demonstrated higher performance, they are highly data-dependent and require a large amount of training images, which remain difficult to be collected for non-RGB images. It is also known that reconstruction-based and dictionary-learning-based methods require high computational memory and cost, which is not desirable for integrated sensor systems.

Manuscript received September 10, 2021; accepted October 6, 2021. Date of publication October 21, 2021; date of current version November 30, 2021. The associate editor coordinating the review of this article and approving it for publication was Dr. Amitava Chatterjee. (Corresponding author: Yusuke Monno.)

The authors are with the Department of Systems and Control Engineering, School of Engineering, Tokyo Institute of Technology, Meguro-ku, Tokyo 152-8550, Japan (e-mail: ymonno@ok.sc.e.titech.ac.jp).

Digital Object Identifier 10.1109/JSEN.2021.3121884

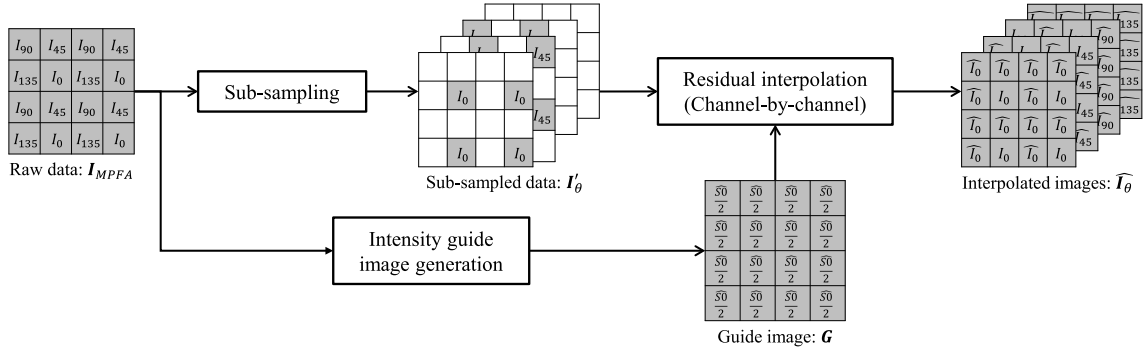


Fig. 1. The outline of our proposed MPFA demosaicking method based on IGRI.

Because of these reasons, interpolation-based methods are still widely applied in practical use because of their simplicity.

In this study, we proposed a novel MPFA demosaicking method based on residual interpolation (RI) [29] and also extended that method to CPFA demosaicking. RI is one of high-performance interpolation methods based on a guide image and has shown its superiority in color demosaicking [29]–[32]. Although RI has also been applied to MPFA demosaicking in some methods [7], [14]–[16], they still do not fully consider the edge information to generate the guide image. In contrast, we proposed a novel intensity-guided RI (IGRI), for which we proposed two intensity guide image generation methods considering four-directional intensity and polarization edge information to effectively interpolate the missing pixel values along the edges. The first method named IGRI-1 incorporates a new edge detector using polarization properties and generates the guide image by considering edge information of north, east, west, and south directions. The second method named IGRI-2 generates the guide image by considering two diagonal, horizontal, and vertical directions using polarization channel correlations. By effectively considering the four-directional edges, our IGRI-based methods achieved high demosaicking performance.

One limitation of MPFA and CPFA demosaicking research is that there are very few public evaluation datasets. Although some recent papers have presented the construction of a color-polarization image dataset, it is captured by a Bayer-patterned camera [25], [33]. Thus, we constructed a new full 12-channel color-polarization image dataset with 40 scenes by using a 3-CCD RGB camera and a polarizer rotated with four orientations. Experimental results using both our new dataset and an existing dataset [25] demonstrated that our IGRI-based methods outperform the best-performed existing interpolation-based method in the recent survey paper [7] and also the state-of-the-art reconstruction-based method [25], [26].

This paper is an extended version of our previous conference paper [34]. In this extended paper, we included a newly proposed guide image generation method as IGRI-2, in addition to IGRI-1 presented in [34]. We also extended our evaluation using both our dataset and Qiu *et al.* dataset [25], while the paper [34] only includes the evaluation using our dataset. Our dataset and source code are publicly available at our website: <http://www.ok.sc.e.titech.ac.jp/res/PolarDem/index.html>.

The rest of this paper is organized as follows. Section II details our proposed MPFA and CPFA demosaicking methods based on two novel guide image generation methods. Section III introduces our newly constructed color-polarization image dataset. Section IV shows experimental results and Section V finally concludes the paper.

II. PROPOSED METHODS

A. MPFA Demosaicking Based on IGRI

Figure 1 shows the outline of our proposed MPFA demosaicking method based on IGRI. To interpolate the missing pixel values in each polarization orientation, we apply RI, which is an interpolation method based on a guide image [29]. In what follows, we first introduce RI and then present two proposed methods for generating an effective intensity guide image from the raw MPFA data.

1) *Residual Interpolation (RI)*: RI performs the interpolation in a residual domain, where the residual is the difference between observed and tentatively estimated pixel values. Figure 2 shows the outline of RI, where the example of I_0 interpolation is shown. As the first step of RI, the tentative estimate is generated by linearly transforming a given guide image G . For each local window $\omega_{p,q}$ centered at the pixel (p, q) , the tentative estimate \check{I}_θ is estimated based on the guided upsampling [35] of the input sub-sampled data I'_θ as

$$\check{I}_\theta(i, j) = a_{p,q}G(i, j) + b_{p,q}, \quad \forall i, j \in \omega_{p,q},$$

$$\theta = \{0, 45, 90, 135\}, \quad (1)$$

where $a_{p,q}$ and $b_{p,q}$ are the linear coefficients to transform the guide image for each local window. Following the Laplacian minimization manner of [29], the linear coefficients are calculated by minimizing the following cost functions.

$$E(a_{p,q}) = \sum_{i,j \in \omega_{p,q}} \left(\tilde{\Delta} I'_\theta(i, j) - a_{p,q} \tilde{\Delta} G^M(i, j) \right)^2, \quad (2)$$

$$E(b_{p,q}) = \sum_{i,j \in \omega_{p,q}} \left(I'_\theta(i, j) - \left(a_{p,q} G^M(i, j) + b_{p,q} \right) \right)^2, \quad (3)$$

where I'_θ is an observed pixel value and G^M is the masked version of the guide image G , for which the mask is defined as one for the sampling pixel positions of I'_θ and zero for other

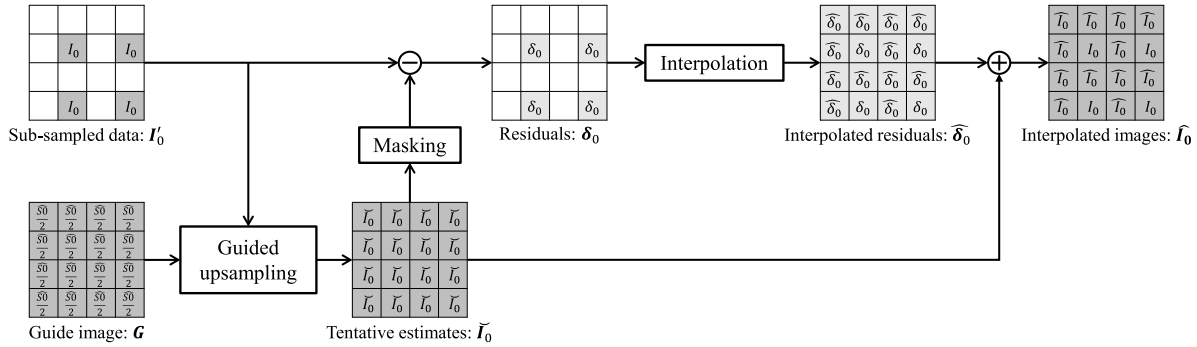


Fig. 2. The outline of RI (an example of I_0 pixel value interpolation).

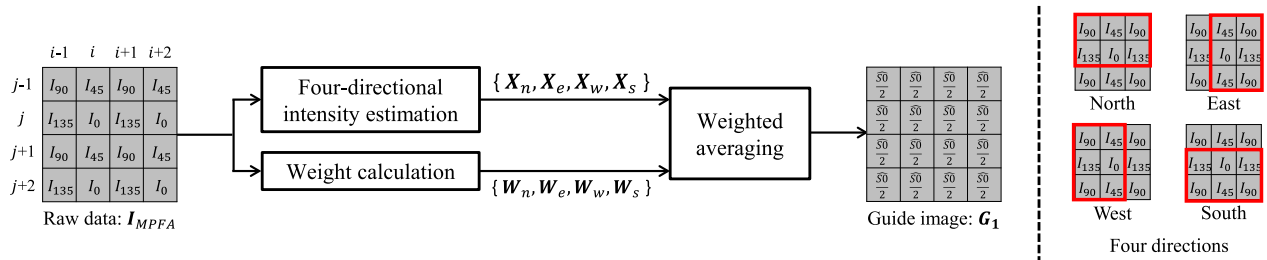


Fig. 3. The outline of our proposed intensity guide image generation for IGRI-1.

positions. The symbol $\tilde{\Delta}$ represents the resultant value of the sparse Laplacian filter, which is defined as

$$\tilde{\Delta} \mathbf{I} = \begin{bmatrix} 0 & 0 & -1 & 0 & 0 \\ 0 & 0 & 0 & 0 & 0 \\ -1 & 0 & 4 & 0 & -1 \\ 0 & 0 & 0 & 0 & 0 \\ 0 & 0 & -1 & 0 & 0 \end{bmatrix} \otimes \mathbf{I}. \quad (4)$$

Following the derivation of [29], Eq. (2) minimizes the Laplacian energy of the residuals, while Eq. (3) minimizes the residuals themselves given the estimated gain component $a_{p,q}$.

The resulting $\check{I}_\theta(i, j)$ values from Eq. (1) are not unique when they are calculated in different sliding windows. Thus, the final tentative estimate is calculated based on the weighted averaging of the linear coefficients within a local window $\omega_{i,j}$ centered at the pixel (i, j) as

$$\check{I}_\theta(i, j) = \bar{a}_{i,j} G(i, j) + \bar{b}_{i,j}, \quad (5)$$

where

$$\bar{a}_{i,j} = \frac{\sum_{p,q \in \omega_{i,j}} W_{p,q} a_{p,q}}{\sum_{p,q \in \omega_{i,j}} W_{p,q}}, \quad (6)$$

$$\bar{b}_{i,j} = \frac{\sum_{p,q \in \omega_{i,j}} W_{p,q} b_{p,q}}{\sum_{p,q \in \omega_{i,j}} W_{p,q}}. \quad (7)$$

The weight $W_{p,q}$ is calculated in the same manner as [29], which is based on the residual cost of Eq. (3) as

$$W_{p,q} = \left(\frac{1}{|\omega_{p,q}|} \sum_{i,j \in \omega_{p,q}} \left(I'_\theta(i, j) - (a_{p,q} G^M(i, j) + b_{p,q}) \right)^2 \right)^{-1} \quad (8)$$

where $|\omega_{p,q}|$ is the number of the sampled I'_θ pixels within the window $\omega_{p,q}$. Equation (8) represents that a high weight is assigned if the residual cost is small.

After generating the tentative estimate \check{I}_θ , the residuals δ_θ at the sampling positions are calculated as

$$\delta_\theta = I'_\theta - \check{I}_\theta^M, \quad (9)$$

where \check{I}_θ^M is the masked version of \check{I}_θ . Finally, the interpolated image \hat{I}_θ is generated by adding the interpolated residuals by bilinear interpolation $\hat{\delta}_\theta$ to the tentative estimate \check{I}_θ as

$$\hat{I}_\theta = \check{I}_\theta + \hat{\delta}_\theta. \quad (10)$$

2) Intensity Guide Image Generation for IGRI-1: Figure 3 shows the outline of our proposed intensity guide image generation for IGRI-1 considering four-directional (i.e., north, east, west, and south) intensity and polarization edges.

We generate the guide image G_1 from raw MPFA data I_{MPFA} by estimating four-directional intensity images and averaging them based on the weights for each direction. By definition, the intensity S_0 , which is one of the Stokes polarization parameters [1], is expressed as

$$S_0 = I_0 + I_{90} = I_{45} + I_{135}, \quad (11)$$

where I_0, I_{45}, I_{90} , and I_{135} are the associated pixel values of the images at four polarization orientations, respectively.

We explain our idea of four-directional estimation, which is inspired by the horizontal-vertical edge detector of [12], by taking the north-direction intensity estimation at pixel (i, j) in Fig. 3 as an example. Based on the definition of Eq. (11),

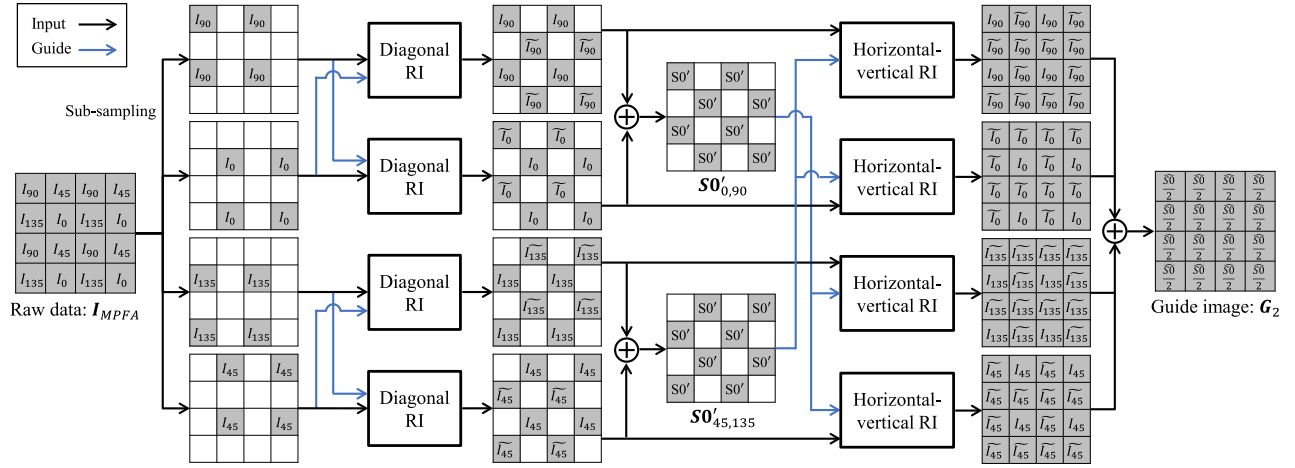


Fig. 4. The outline of our proposed intensity guide image generation for IGRI-2.

for the north region, we estimate the intensity of pixel (i, j) by

$$\begin{aligned} \widehat{S\bar{O}}_{n(0,90)}(i, j) &= I_0(i, j) + \frac{1}{2} (I_{90}(i-1, j-1) \\ &\quad + I_{90}(i+1, j-1)), \\ \widehat{S\bar{O}}_{n(45,135)}(i, j) &= I_{45}(i, j-1) + \frac{1}{2} (I_{135}(i-1, j) \\ &\quad + I_{135}(i+1, j)), \end{aligned} \quad (12)$$

where suffix n represents the north region, $\widehat{S\bar{O}}_{n(0,90)}$ and $\widehat{S\bar{O}}_{n(45,135)}$ are the estimated intensities using (I_0, I_{90}) and (I_{45}, I_{135}) , respectively. We then calculate the average and the difference of the two estimates as

$$\widehat{S\bar{O}}_n(i, j) = \frac{1}{2} (\widehat{S\bar{O}}_{n(0,90)}(i, j) + \widehat{S\bar{O}}_{n(45,135)}(i, j)), \quad (13)$$

$$\Delta \widehat{S\bar{O}}_n(i, j) = \widehat{S\bar{O}}_{n(0,90)}(i, j) - \widehat{S\bar{O}}_{n(45,135)}(i, j). \quad (14)$$

If there are no intensity edges and polarization edges (i.e., edges caused by the polarization parameter differences between pixels) in the region, the difference of Eq. (14) becomes zero, meaning that the intensity of Eq. (13) is estimated without crossing the edges. Thus, we evaluate the intensity differences for four directions (i.e., north, east, west, and south in Fig. 3) to determine the weights of interpolation directions for generating the intensity guide image.

The four-directional intensity estimates and intensity differences can be calculated by filtering the raw MPFA data I_{MPFA} . The directional intensity estimate $X_k = \widehat{S\bar{O}}_k/2$, which is normalized to the pixel value range, is calculated as

$$X_k = F_k \otimes I_{MPFA}, \quad k = \{n, e, w, s\}, \quad (15)$$

where \otimes represents the filtering operation and k represents the direction of north (n), east (e), west (w), and south (s). F_k is

the filter kernel for k -direction, which is expressed as

$$\begin{aligned} F_n &= \begin{bmatrix} 1/8 & 1/4 & 1/8 \\ 1/8 & 1/4 & 1/8 \\ 0 & 0 & 0 \end{bmatrix}, \quad F_e = \begin{bmatrix} 0 & 1/8 & 1/8 \\ 0 & 1/4 & 1/4 \\ 0 & 1/8 & 1/8 \end{bmatrix}, \\ F_w &= \begin{bmatrix} 1/8 & 1/8 & 0 \\ 1/4 & 1/4 & 0 \\ 1/8 & 1/8 & 0 \end{bmatrix}, \quad F_s = \begin{bmatrix} 0 & 0 & 0 \\ 1/8 & 1/4 & 1/8 \\ 1/8 & 1/4 & 1/8 \end{bmatrix}. \end{aligned} \quad (16)$$

The directional intensity difference $\Delta \widehat{S\bar{O}}_k$ is calculated as

$$\Delta \widehat{S\bar{O}}_k = H_k \otimes I_{MPFA}, \quad (17)$$

where each filter kernel H_k is expressed as

$$\begin{aligned} H_n &= \begin{bmatrix} -1/2 & 1 & -1/2 \\ 1/2 & -1 & 1/2 \\ 0 & 0 & 0 \end{bmatrix}, \quad H_e = \begin{bmatrix} 0 & 1/2 & 1/2 \\ 0 & -1 & 1 \\ 0 & 1/2 & -1/2 \end{bmatrix}, \\ H_w &= \begin{bmatrix} -1/2 & 1/2 & 0 \\ 1 & -1 & 0 \\ -1/2 & 1/2 & 0 \end{bmatrix}, \quad H_s = \begin{bmatrix} 0 & 0 & 0 \\ 1/2 & -1 & 1/2 \\ -1/2 & 1 & -1/2 \end{bmatrix}. \end{aligned} \quad (18)$$

We then calculate the weight for each direction as

$$W_k(i, j) = \frac{1}{\Delta \widehat{S\bar{O}}'_k(i, j) + \varepsilon}, \quad (19)$$

$$\Delta \widehat{S\bar{O}}'_k = D_k \otimes |\Delta \widehat{S\bar{O}}_k| \quad (20)$$

where D_k is the 5×5 -sized smoothing kernel for k -direction, ε is a small positive value (set as 10^{-32}) to avoid the division by zero, and $|\cdot|$ represents the element-wise absolute value operator.

The intensity guide image G_1 is then generated by the pixel-wise weighted averaging of $X_k(i, j)$ as

$$G_1(i, j) = \sum_{k=n,e,w,s} W_k(i, j) X_k(i, j) / \sum_{k=n,e,w,s} W_k(i, j). \quad (21)$$

Using the generated guide image G_1 , we apply RI to interpolate the missing pixel values, as explained in Section II-A.1.

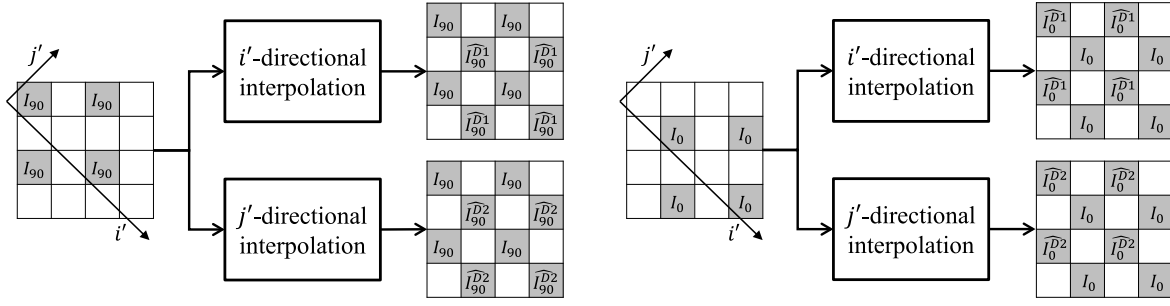


Fig. 5. Initial interpolation for generating guides for diagonal directions.

3) *Intensity Guide Image Generation for IGRI-2*: Figure 4 shows the outline of our proposed intensity guide image generation for IGRI-2 considering the intensity and polarization edges of the two-diagonal and the horizontal-vertical directions. We generate the guide image G_2 with two-step interpolation by combining diagonal RI and horizontal-vertical RI, which is inspired by the green-channel interpolation for color demosaicking in [29]. The key observation of IGRI-2 is that we can estimate the intensity in diagonal directions according to the relationship of Eq. (11) because either (I_0, I_{90}) or (I_{45}, I_{135}) pair is aligned diagonally in the raw MPFA data.

For the first-step interpolation, we apply diagonal RI to interpolate missing I_{90} values at the I_0 pixel positions. Similarly, diagonal RI is also applied to interpolate the missing I_0 values at the I_{90} pixel positions. Then, the diagonally interpolated I_{90} and I_0 values are added to generate the intensity $SO'_{0,90}$, which is used as the guide information for the next horizontal-vertical RI. Similarly, the intensity $SO'_{45,135}$ is generated using the diagonally interpolated I_{45} and I_{135} values.

For the second-step interpolation, we interpolate the remaining missing pixel values by horizontal-vertical RI, in which $SO'_{0,90}$ is used as the guide for interpolating I_{45} and I_{135} values, while $SO'_{45,135}$ is used as the guide for interpolating I_0 and I_{90} values. The interpolated four orientation images are then averaged to generate the intensity guide image G_2 . Below, we detail each step of the diagonal RI. The horizontal-vertical RI is performed in the same manner as the diagonal RI with only the difference of the interpolation directions.

The first step of the diagonal RI is generating the guides for diagonal directions. Figure 5 illustrates the initial interpolation for generate the guide from I_{90} and I_0 data, which is performed by linear interpolation along the two diagonal directions (D_1, D_2) represented by (i', j') pixel coordinate. The interpolated I_{90} values at the I_0 positions are calculated as

$$\begin{aligned} \hat{I}_{90}^{D1}(i', j') &= \frac{1}{2} (I_{90}(i' - 1, j') + I_{90}(i' + 1, j')), \\ \hat{I}_{90}^{D2}(i', j') &= \frac{1}{2} (I_{90}(i', j' - 1) + I_{90}(i', j' + 1)), \end{aligned} \quad (22)$$

where pixel (i', j') corresponds to a target pixel at the I_0 pixel positions. The I_0 values at the I_{90} pixel positions are similarly calculated by the linear interpolation.

Figure 6 shows the outline of the diagonal RI by taking the I_{90} pixel value interpolation at the I_0 pixels as an example. Given the generated diagonal guide \hat{I}_0^{D1} as explained above, the i -directional RI of I_{90} is performed to obtain the diagonally interpolated data \tilde{I}_{90}^{D1} . Similarly, the i -directional RI of I_0 is performed to obtain \tilde{I}_0^{D1} . The i -directional RI is performed in the same manner as the processes explained in Section II-A.1 by considering only the diagonal samples and applying the one-dimensional sparse Laplacian filter of $[-1 \ 0 \ 2 \ 0 \ -1]$. The j -directional RI is also performed in the same manner to obtain \tilde{I}_{90}^{D2} and \tilde{I}_0^{D2} .

After generating the diagonally interpolated data, the intensity differences for two diagonal directions are calculated as follows.

$$\tilde{\delta}_{90,0}^{D1}(i', j') = \begin{cases} \tilde{I}_{90}^{D1}(i', j') - I_0(i', j'), & \text{at } I_0 \text{ pixels} \\ I_{90}(i', j') - \tilde{I}_0^{D1}(i', j'), & \text{at } I_{90} \text{ pixels} \end{cases} \quad (23)$$

$$\tilde{\delta}_{90,0}^{D2}(i', j') = \begin{cases} \tilde{I}_{90}^{D2}(i', j') - I_0(i', j'), & \text{at } I_0 \text{ pixels} \\ I_{90}(i', j') - \tilde{I}_0^{D2}(i', j'), & \text{at } I_{90} \text{ pixels} \end{cases} \quad (24)$$

These two diagonal intensity differences are smoothed and combined as

$$\begin{aligned} \tilde{\delta}_{90,0}(i', j') &= \{\omega_1 * f_1 * \tilde{\delta}_{90,0}^{D2}(i' - 3 : i', j') \\ &\quad + \omega_2 * f_2 * \tilde{\delta}_{90,0}^{D2}(i' : i' + 3, j') \\ &\quad + \omega_3 * \tilde{\delta}_{90,0}^{D1}(i', j' - 3 : j') * f_1^T \\ &\quad + \omega_4 * \tilde{\delta}_{90,0}^{D1}(i', j' : j' + 3) * f_2^T\} / \omega, \\ \omega &= \omega_1 + \omega_2 + \omega_3 + \omega_4, \end{aligned} \quad (25)$$

where f_1 and f_2 are smoothing filter kernels and $\{\omega_1, \omega_2, \omega_3, \text{ and } \omega_4\}$ are the weights for combining diagonal intensity differences. For these smoothing and weighted averaging processes, we follow the same processes as in the reference [29]. The Gaussian smoothing weights are set as

$$\begin{aligned} f_1 &= [0.01, 0.08, 0.35, 0.56], \\ f_2 &= [0.56, 0.35, 0.08, 0.01], \end{aligned} \quad (26)$$

and the weights for each direction are calculated using intensity difference gradients in the diagonal directions as

$$\omega_1 = 1 / \left(\sum_{a=i'-2}^{i'} \sum_{b=j'-1}^{j'+1} V_{a,b}^{D2} \right)^2,$$

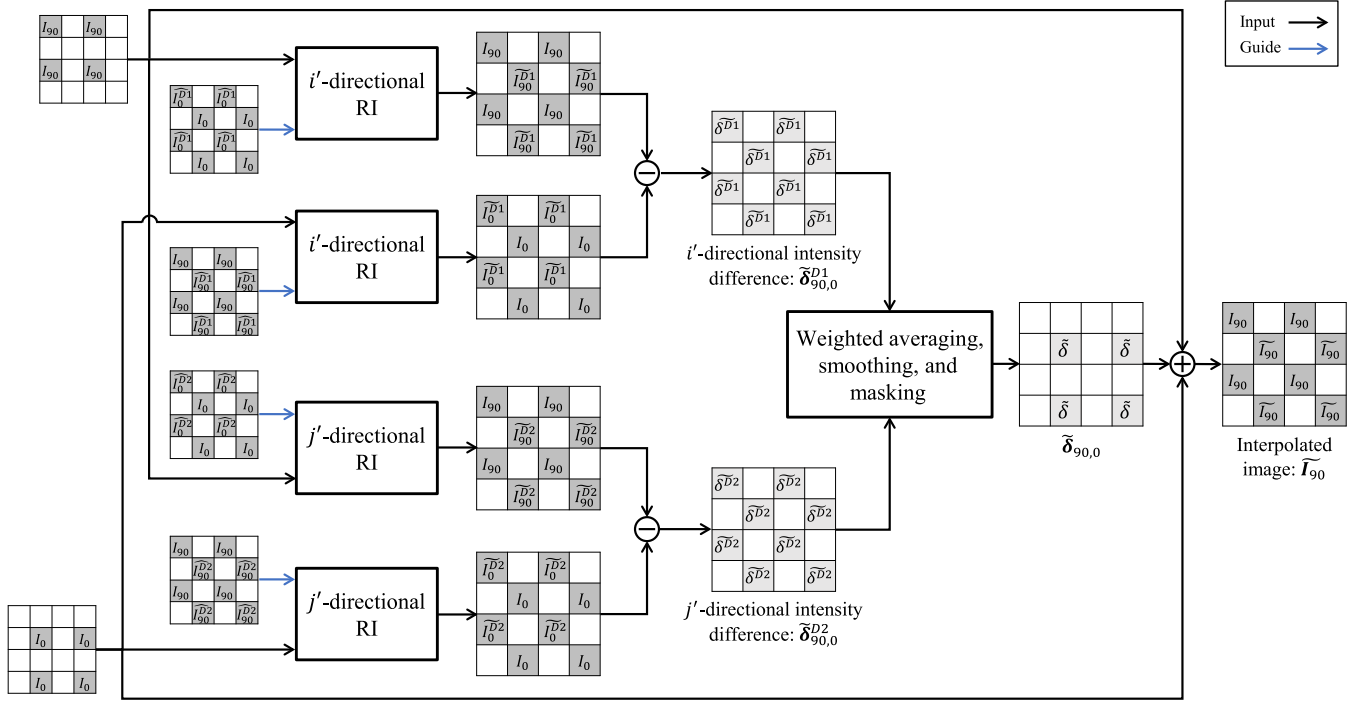


Fig. 6. The outline of diagonal RI (an example of I_{90} pixel value interpolation at I_0 pixels).

$$\begin{aligned} \omega_2 &= 1 / \left(\sum_{a=i'+2}^{i'+1} \sum_{b=j'-1}^{j'+1} V_{a,b}^{D2} \right)^2, \\ \omega_3 &= 1 / \left(\sum_{a=i'-1}^{i'+1} \sum_{b=j'}^{j'+2} V_{a,b}^{D1} \right)^2, \\ \omega_4 &= 1 / \left(\sum_{a=i'-1}^{i'+1} \sum_{b=j'-2}^{j'} V_{a,b}^{D1} \right)^2, \end{aligned} \quad (27)$$

where the directional gradients are calculated as

$$\begin{aligned} V^{D1}(i', j') &= \|\tilde{\delta}^{D1}(i', j' - 1) - \tilde{\delta}^{D1}(i', j' + 1)\|, \\ V^{D2}(i', j') &= \|\tilde{\delta}^{D2}(i' - 1, j') - \tilde{\delta}^{D2}(i' + 1, j')\|. \end{aligned} \quad (28)$$

Finally, we obtain the interpolated I_{90} pixel value at the I_0 pixel by adding the observed I_0 pixel value to the combined intensity difference as

$$\tilde{I}_{90}(i', j') = I_0(i', j') + \tilde{\delta}_{90,0}^M(i', j'), \quad (29)$$

where $\tilde{\delta}^M$ is the masked version of $\tilde{\delta}$. After the diagonal RI, the horizontal-vertical RI is performed in the same manner to obtain the fully interpolated I_{90} image.

The interpolation of other polarization orientations I_0 , I_{45} , and I_{135} are also performed in the same manner as that of I_{90} . The interpolated images of four directions are then averaged to generate the intensity guide image G_2 . Then, we finally apply RI using the guide image G_2 to interpolate the missing pixel values, as explained in Section II-A.1.

B. Extension to CPFA Demosaicking

We here extend our proposed MPFA demosaicking method to CPFA demosaicking. Figure 7 shows the outline of our proposed CPFA demosaicking framework, which effectively combines existing color and our MPFA demosaicking methods. We first sub-sample and down-sample (as expressed by $\downarrow 2$) the raw CPFA data to obtain Bayer-patterned data of four orientations. We then apply an existing color demosaicking method to each Bayer-patterned data. The four demosaicked RGB images are then up-sampled (as expressed by $\uparrow 2$) and aligned to form the MPFA data of each color channel. Finally, we apply our MPFA demosaicking method to each MPFA data to obtain full 12-channel color-polarization images.

III. COLOR POLARIZATION IMAGE DATASET

A. Dataset Capturing

We newly constructed a full 12-channel color-polarization image dataset with 40 scenes, as shown in Fig. 8. Each 12-channel data consists of four RGB images captured with four polarizer angles of 0, 45, 90, and 135 degrees, as shown in Fig. 8(b). We used JAI CV-M9GE 3-CCD camera and SIGMAKOKI SPF-50C-32 linear polarizer attached to PH-50-ARS rotating polarizer mount. As shown in Fig. 8(a), each 12-channel data were captured by rotating the linear polarizer placed in front of the camera under an unpolarized light condition. For each polarizer orientation, we captured 1,000 images and averaged them to make the ground-truth image with reduced noise, as performed in [36]. The image resolution is 1024×768 with 10-bit depth.

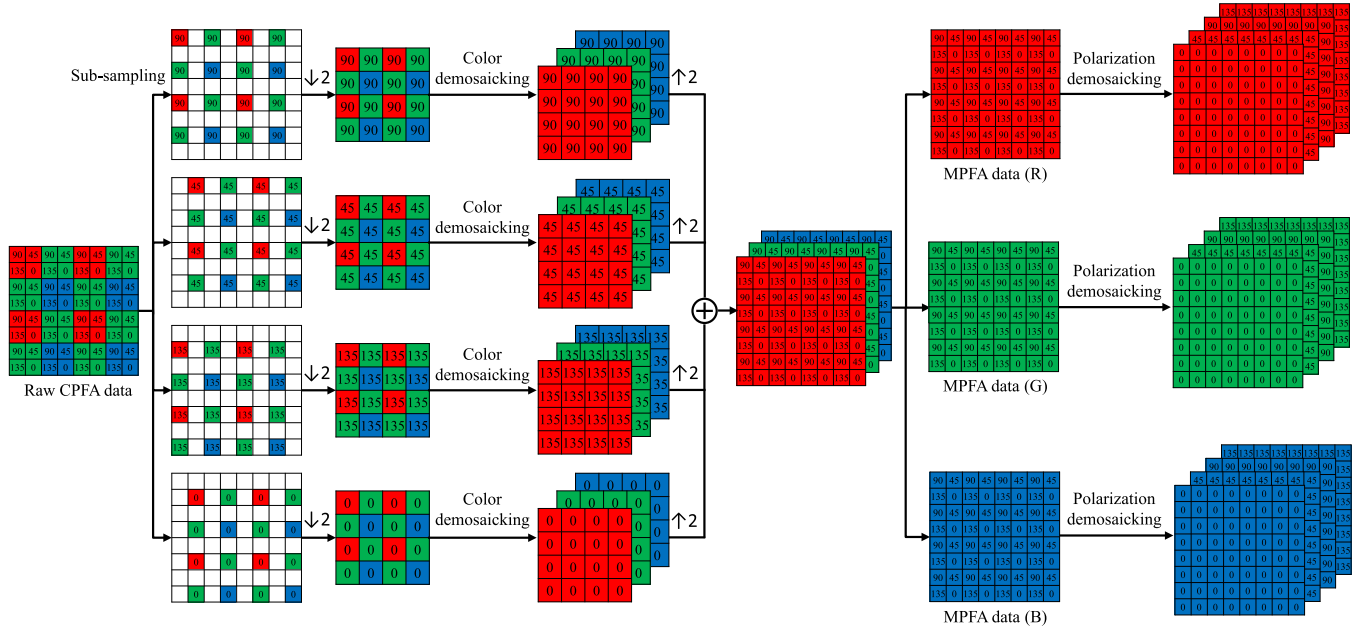


Fig. 7. The outline of our proposed CPFA demosaicking method.

B. AoP-DoP Visualization

To effectively show the experimental results, we simultaneously visualized AoP and DoP, as shown in Fig. 8(b). For each pixel, Stokes parameters were firstly calculated from the four orientation pixel values I_0 , I_{45} , I_{90} , and I_{135} obtained through the polarizer at 0, 45, 90, and 135 orientations as

$$S = \begin{bmatrix} S_0 \\ S_1 \\ S_2 \end{bmatrix} = \begin{bmatrix} (I_0 + I_{45} + I_{90} + I_{135})/2 \\ I_0 - I_{90} \\ I_{45} - I_{135} \end{bmatrix}, \quad (30)$$

where we assumed linear polarization, i.e., $S_3 = 0$ and used all four orientation images for S_0 to reduce the noise. Then, AoP and DoP were calculated as

$$DoP = \frac{\sqrt{S_1^2 + S_2^2}}{S_0}, \quad (31)$$

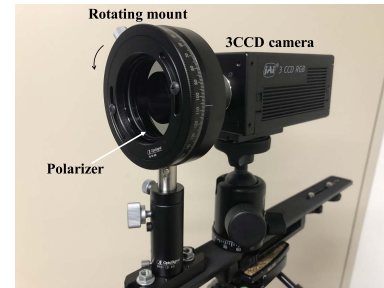
$$AoP = \frac{1}{2} \tan^{-1} \frac{S_2}{S_1}. \quad (32)$$

We visualized AoP and DoP by the HSV color space, where ‘‘Hue’’ corresponds to AoP and ‘‘Saturation’’ corresponds to DoP. For ‘‘Saturation’’, we used DoP^2 to highlight the regions that have larger DoP values, which have more meaningful information for applications using polarization images.

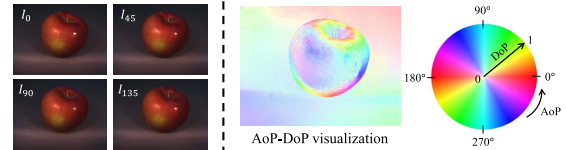
IV. EXPERIMENTAL RESULTS

A. MPFA Demosaicking Results

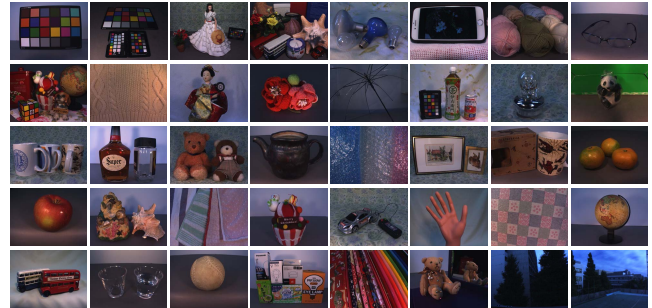
We first evaluated the performance of our MPFA demosaicking methods using our dataset and a public dataset constructed by Qiu *et al.* [25], [26]. Both our dataset and Qiu *et al.* dataset contain 12-channel color-polarization images of 40 scenes. We used the green-channel images of the color-polarization dataset as ground-truth monochrome polarization images. We compared our IGRI-based methods with four interpolation-based methods: bilinear, bicubic, ICPC [12], and PPID [7].



(a) Setup for obtaining the dataset



(b) Example color-polarization image set and its AoP-DoP visualization



(c) 40 scenes in the dataset

Fig. 8. Our full 12-channel color-polarization image dataset.

The PPID method is based on a guide image called a pseudo-panchromatic image [37] and presents the best performance among the interpolation-based methods compared in the recent

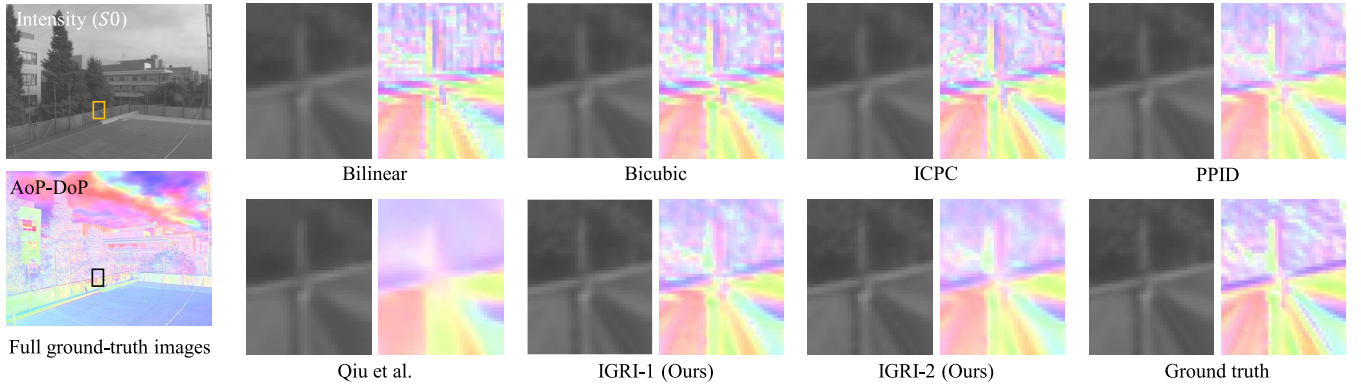


Fig. 9. Visual comparison of the intensity image and the AoP-DoP visualization for MPFA demosaicking (our dataset).

TABLE I
NUMERICAL COMPARISON FOR MPFA DEMOSAICKING (AVERAGE OF 40 SCENES IN OUR DATASET)

Method	PSNR								Angle error
	I_0	I_{45}	I_{90}	I_{135}	S_0	S_1	S_2	DoP	AoP
Bilinear	42.34	41.58	42.50	41.58	44.89	46.14	45.03	33.70	21.36
Bicubic	43.45	42.48	43.63	42.48	46.22	47.00	45.73	34.46	20.64
ICPC [12]	43.10	42.22	43.23	42.22	45.78	47.01	45.73	34.75	20.50
PPID [7]	46.52	44.52	46.91	44.34	48.94	50.56	47.59	36.96	17.65
Qiu et al. [25]	-	-	-	-	46.71	52.13	46.13	34.23	18.50
IGRI-1 (Ours)	47.39	44.91	47.84	44.63	49.62	51.48	47.83	36.79	17.13
IGRI-2 (Ours)	47.82	45.04	48.50	44.56	49.82	52.39	47.45	36.37	17.03

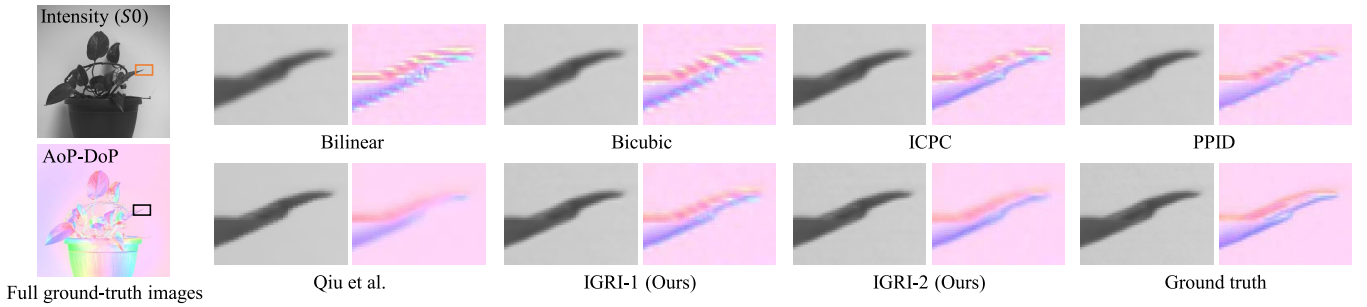


Fig. 10. Visual comparison of the intensity image and the AoP-DoP visualization for MPFA demosaicking (Qiu *et al.* dataset).

TABLE II
NUMERICAL COMPARISON FOR MPFA DEMOSAICKING (AVERAGE OF 40 SCENES IN QIU *et al.* DATASET)

Method	PSNR								Angle error
	I_0	I_{45}	I_{90}	I_{135}	S_0	S_1	S_2	DoP	AoP
Bilinear	43.82	45.13	45.43	44.14	47.57	47.83	48.04	38.05	11.20
Bicubic	44.27	45.59	45.90	44.58	48.20	48.19	48.39	38.49	11.32
ICPC [12]	44.34	45.69	45.99	44.67	48.24	48.38	48.60	38.74	11.00
PPID [7]	46.26	47.53	47.68	46.68	50.17	50.37	50.72	40.67	10.03
Qiu et al. [25]	-	-	-	-	48.90	50.96	51.58	40.26	9.46
IGRI-1 (Ours)	46.69	47.98	48.14	47.12	50.61	50.89	51.22	41.00	9.93
IGRI-2 (Ours)	47.69	49.13	49.28	48.17	51.89	51.63	52.02	41.57	9.63

survey paper [7]. We also compared our methods with a recently proposed state-of-the-art reconstruction-based method proposed by Qiu *et al.* [25], [26].

Figure 9 and 10 show the visual comparisons with our dataset and Qiu *et al.* dataset, where the S_0 image and the AoP-DoP visualization are shown. The results for both datasets show that the existing interpolation-based methods generate severe edge artifacts and Qiu *et al.* reconstruction-based method fails to clearly reconstruct the edges and generates blurry results. In contrast, our IGRI methods reconstruct the edges more clearly with reduced artifacts. Especially for

diagonal edges, our IGRI-2 method shows a significantly better result and generates the closest result to the ground truth. These results validate that our IGRI methods can effectively exploit high-quality intensity guide images considering four-directional edges.

Table I and II show the numerical comparisons with our dataset and Qiu *et al.* dataset, where we evaluated the average root mean square error (RMSE) of the angle errors for AoP images and the average peak signal-to-noise ratio (PSNR) for four polarization images (I_0 , I_{45} , I_{90} , and I_{135}), three Stokes parameter images (S_0 , S_1 , S_2), and DoP images.

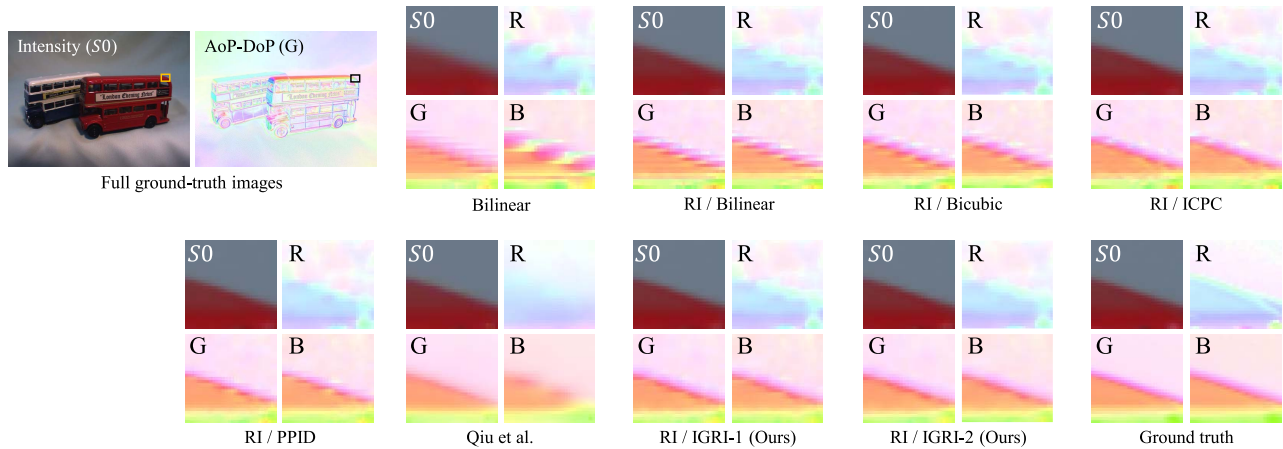


Fig. 11. Visual comparison of the intensity image and the AoP-DoP visualization for CPFA demosaicking (our dataset).

TABLE III
NUMERICAL COMPARISON FOR CPFA DEMOSAICKING (AVERAGE OF 40 SCENES IN OUR DATASET)

Method (color polarization)		CPSNR							Angle error	
		I_0	I_{45}	I_{90}	I_{135}	S_0	S_1	S_2	DoP	AoP
Bilinear		35.32	34.94	35.47	35.00	36.31	43.29	41.28	31.20	24.98
Qiu <i>et al.</i> [25]		-	-	-	-	37.48	47.04	42.47	31.90	20.98
RI	Bilinear	38.34	37.79	38.50	37.86	40.03	44.09	42.58	31.96	24.15
	Bicubic	38.65	38.05	38.81	38.12	40.43	44.30	42.72	32.05	24.11
	ICPC [12]	38.61	38.01	38.77	38.09	40.33	44.49	42.87	32.36	23.86
	PPID [7]	39.37	38.68	39.57	38.71	40.73	46.34	44.04	33.98	22.40
	IGRI-1 (Ours)	39.41	38.72	39.62	38.72	40.76	46.49	44.10	33.74	22.18
IGRI-2 (Ours)		39.43	38.72	39.68	38.70	40.54	47.30	44.33	34.00	21.63

The PSNR values of Qiu *et al.* method for four polarization images (I_0 , I_{45} , I_{90} , and I_{135}) are blank, since the direct outputs of Qiu *et al.* method are the Stokes parameters, AoP, and DoP images, instead of 12-channel color-polarization images. A higher PSNR value and a lower angle RMSE mean better performance.

From Table I and II, we can see that our IGRI methods generally show better performance in most parameters. For the four polarization images (I_0 , I_{45} , I_{90} , and I_{135}) and the intensity (S_0) image, our IGRI-2 method achieves significant improvement compared with the existing methods. This performance improvement is mainly derived from the interpolation performance for diagonal edges, which can be visually seen in the results of the AoP-DoP visualization in Fig 9 and 10, because the IGRI-2 method effectively considers the diagonal directions in addition to horizontal-vertical directions. Although the best-performing methods for AoP and DoP evaluation are not consistent, we can confirm that the IGRI-1 and the IGRI-2 methods show a better balance for our dataset and Qiu *et al.* dataset, respectively, in terms of the average performance for AoP and DoP. Although Qiu *et al.* method shows the best result for AoP in Table II, their reconstruction-based method takes longer computational time than our IGRI methods. By non-optimized MATLAB codes, our IGRI-1 and IGRI-2 methods take approximately 2 seconds and 40 seconds, respectively, to process 1024×768 pixel data, while the MATLAB code of Qiu *et al.* method takes approximately 120 seconds. Comparing the IGRI-1 and the IGRI-2 methods, the IGRI-2 method generally provides better

performance at the cost of increased computational time. The IGRI-1 method shows a better trade-off between the performance and the computational time.

B. CPFA Demosaicking Results

We next evaluated the performance of CPFA demosaicking using the full 12-channel color-polarization image datasets. We applied RI [29] for the color demosaicking step and compared our IGRI methods with the same MPFA demosaicking methods as presented in the previous subsection. We also compared our methods with the bilinear interpolation and the state-of-the-art reconstruction-based method of Qiu *et al.* These two methods are one-step methods that directly estimate the final outputs, where Qiu *et al.* method directly estimates Stokes parameters instead of 12-channel color-polarization images.

Figure 11 and 12 show the visual comparisons with our dataset and Qiu *et al.* dataset [25], [26]. In the visual comparison, our IGRI methods show better results, though there still exist some jaggy artifacts, since the CPFA demosaicking is very challenging due to the very sparse nature of each color-polarization sample. Similar to the MPFA demosaicking, for diagonal edges, our IGRI-2 method shows substantially better results than other methods and generates the closest result to the ground truth.

Table III and IV show the numerical comparisons with our dataset and Qiu *et al.* dataset. These results show the average color PSNR (CPSNR) and the average angle RMSE (the average of RGB) for CPFA demosaicking. The results

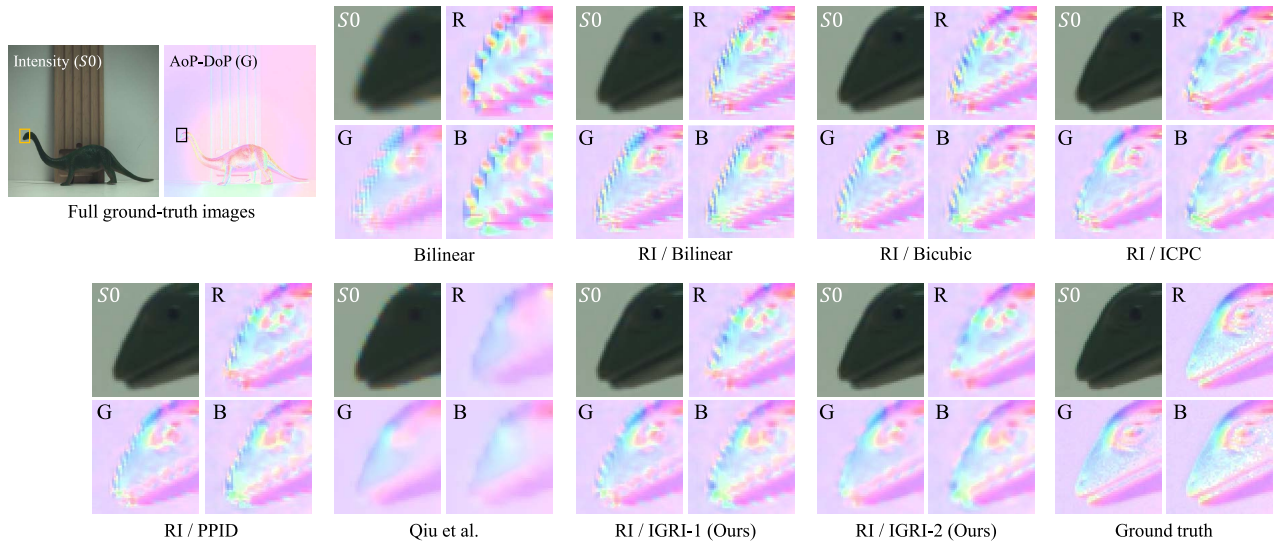


Fig. 12. Visual comparison of the intensity image and the AoP-DoP visualization for CPFA demosaicking (Qiu *et al.* dataset).

TABLE IV
NUMERICAL COMPARISON FOR CPFA DEMOSAICKING (AVERAGE OF 40 SCENES IN QIU *et al.* DATASET)

Method (color polarization)		CPSNR							Angle error	
		I_0	I_{45}	I_{90}	I_{135}	S_0	S_1	S_2	DoP	AoP
Bilinear		38.99	40.15	40.35	39.27	41.17	45.36	45.85	35.46	12.77
Qiu et al. [25]		-	-	-	-	42.72	47.65	48.40	37.01	11.14
RI	Bilinear	42.41	43.50	43.73	42.68	45.74	46.84	47.11	36.98	12.51
	Bicubic	42.65	43.74	43.97	42.92	46.09	47.02	47.29	37.19	12.59
	ICPC [12]	42.78	43.88	44.10	43.06	46.17	47.24	47.52	37.45	12.36
	PPID [7]	43.72	44.80	44.97	44.05	46.93	48.56	48.93	38.75	11.68
	IGRI-1 (Ours)	43.81	44.89	45.04	44.12	46.96	48.73	49.10	38.77	11.62
IGRI-2 (Ours)		44.23	45.35	45.51	44.57	47.27	49.28	49.69	39.29	11.26

show the similar trends to the results of MPFA demosaicking, as detailed in the previous subsection, and our IGRI-1 and IGRI-2 methods show a better average performance compared with existing methods. Comparing the PPID and our IGIR methods, we can observe close results in some of the parameters. Since the PPID and our IGRI methods adopted the same RI method [29] for the first color demosaicking step, the final performance could be bounded by the performance of the first step. Even though, the PPID method shows weak interpolation performance for diagonal edges and generates more jaggy artifacts, which distort the visual perception as shown in Fig. 11 and 12 and also may degrade the performance of potential applications. Although Qiu *et al.* method shows the best performance for AoP, their method is more time-consuming compared with our IGRI methods as explained in the previous subsection.

C. Results for a Real Sensor

To demonstrate an application for a real sensor, we applied our IGRI-2 method to the raw CPFA data captured using a LUCID VP-PHX-050S-Q color polarization camera with 2448×2048 pixel resolution. Figure 13 shows the examples of an intensity image, an I_{min} image, and AoP-DoP visualization of the G channel, which were generated from the 12-channel color-polarization images demosaicked by our proposed method. These examples show that our method

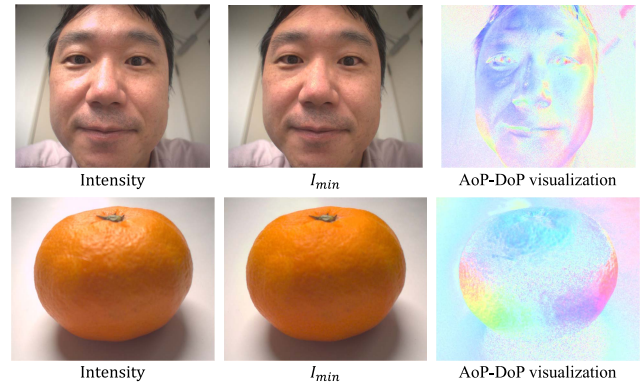


Fig. 13. Examples of real sensor images generated from the demosaicked 12-channel color-polarization images by our IGRI-2 method.

generates high-quality results for a real color polarization sensor. We can see that the I_{min} image can remove the specular reflection components, which is one of the demanded applications in image processing and computer vision fields.

V. CONCLUSION

In this paper, we have proposed two MPFA demosaicking methods based on IGRI, where we have proposed two effective intensity guide image generation methods for IGRI considering four-directional intensity and polarization edge informa-

tion. We have also proposed CPFA demosaicking methods by combining the proposed MPFA demosaicking methods and an existing color demosaicking method. We have newly constructed a full 12-channel color-polarization image dataset of 40 scenes by using a rotating polarizer and a 3-CCD RGB camera and have evaluated the proposed MPFA and CPFA demosaicking methods using the constructed dataset and Qiu *et al.* dataset [25]. Experimental results have demonstrated that our proposed MPFA and CPFA demosaicking methods show better performance compared with other existing methods in both quantitative and qualitative evaluation.

REFERENCES

- [1] E. Collett, *Field Guide to Polarization*. Bellingham, WA, USA: SPIE, 2005.
- [2] L. V. Jospin, G. Baechler, and A. Scholefield, "Embedded polarizing filters to separate diffuse and specular reflection," in *Proc. Asian Conf. Comput. Vis. (ACCV)*, 2018, pp. 3–18.
- [3] P. Wieschollek, O. Gallo, J. Gu, and J. Kautz, "Separating reflection and transmission images in the wild," in *Proc. Eur. Conf. Comput. Vis. (ECCV)*, 2018, pp. 89–104.
- [4] Z. Cui, J. Gu, B. Shi, P. Tan, and J. Kautz, "Polarimetric multi-view stereo," in *Proc. IEEE Conf. Comput. Vis. Pattern Recognit. (CVPR)*, Jul. 2017, pp. 1558–1567.
- [5] J. Zhao, Y. Monno, and M. Okutomi, "Polarimetric multi-view inverse rendering," in *Proc. Eur. Conf. Comput. Vis. (ECCV)*, 2020, pp. 85–102.
- [6] J. S. Tyo, D. L. Goldstein, D. B. Chenault, and J. A. Shaw, "Review of passive imaging polarimetry for remote sensing applications," *Appl. Opt.*, vol. 45, no. 22, pp. 5453–5469, 2006.
- [7] S. Mihoubi, P.-J. Lapray, and L. Bigué, "Survey of demosaicking methods for polarization filter array images," *Sensors*, vol. 18, no. 11, p. 3688, Oct. 2018.
- [8] Y. Maruyama *et al.*, "3.2-MP back-illuminated polarization image sensor with four-directional air-gap wire grid and 2.5- μm pixels," *IEEE Trans. Electron Devices*, vol. 65, no. 6, pp. 2544–2551, May 2018.
- [9] B. M. Ratliff, C. F. Lacasse, and J. S. Tyo, "Interpolation strategies for reducing IFOV artifacts in microgrid polarimeter imagery," *Opt. Exp.*, vol. 17, no. 11, pp. 9112–9125, 2009.
- [10] S. Gao and V. Gruev, "Bilinear and bicubic interpolation methods for division of focal plane polarimeters," *Opt. Exp.*, vol. 19, no. 27, pp. 26161–26173, 2011.
- [11] S. Gao and V. Gruev, "Gradient-based interpolation method for division-of-focal-plane polarimeters," *Opt. Exp.*, vol. 21, pp. 1137–1151, Jan. 2013.
- [12] J. Zhang, H. Luo, B. Hui, and Z. Chang, "Image interpolation for division of focal plane polarimeters with intensity correlation," *Opt. Exp.*, vol. 24, no. 18, pp. 20799–20807, 2016.
- [13] N. Li, Y. Zhao, Q. Pan, and S. G. Kong, "Demosaicking DoFP images using Newton's polynomial interpolation and polarization difference model," *Opt. Exp.*, vol. 27, no. 2, pp. 1376–1391, 2019.
- [14] A. Ahmed, X. Zhao, V. Gruev, J. Zhang, and A. Bermak, "Residual interpolation for division of focal plane polarization image sensors," *Opt. Exp.*, vol. 25, no. 9, pp. 10651–10662, 2017.
- [15] A. Ahmed, X. Zhao, J. Chang, H. Ma, V. Gruev, and A. Bermak, "Four-directional adaptive residual interpolation technique for DoFP polarimeters with different micro-polarizer patterns," *IEEE Sensors J.*, vol. 18, no. 19, pp. 7990–7997, Oct. 2018.
- [16] T. Jiang *et al.*, "Minimized Laplacian residual interpolation for DoFP polarization image demosaicking," *Appl. Opt.*, vol. 58, no. 27, pp. 7367–7374, Sep. 2019.
- [17] Z. Jiang, Q. Zhang, S. Wu, T. Xu, Y. Su, and C. Bai, "Reconstructing Stokes parameters from non-uniform division-of-focal-plane modulation," *Opt. Lasers Eng.*, vol. 134, Nov. 2020, Art. no. 106199.
- [18] S. Liu, J. Chen, Y. Xun, X. Zhao, and C.-H. Chang, "A new polarization image demosaicking algorithm by exploiting inter-channel correlations with guided filtering," *IEEE Trans. Image Process.*, vol. 29, pp. 7076–7089, 2020.
- [19] R. Wu, Y. Zhao, N. Li, and S. G. Kong, "Polarization image demosaicking using polarization channel difference prior," *Opt. Exp.*, vol. 29, no. 14, pp. 22066–22079, 2021.
- [20] J. Zhang *et al.*, "Sparse representation-based demosaicking method for microgrid polarimeter imagery," *Opt. Lett.*, vol. 43, no. 14, pp. 3265–3268, 2018.
- [21] J. Zhang, J. Chen, H. Yu, D. Yang, B. Liang, and M. Xing, "Polarization image demosaicking via nonlocal sparse tensor factorization," *IEEE Trans. Geosci. Remote Sens.*, early access, Jul. 15, 2021, doi: 10.1109/TGRS.2021.3093903.
- [22] J. Zhang *et al.*, "Learning a convolutional demosaicking network for microgrid polarimeter imagery," *Opt. Lett.*, vol. 43, no. 18, pp. 4534–4537, 2018.
- [23] X. Zeng, Y. Luo, X. Zhao, and W. Ye, "An end-to-end fully-convolutional neural network for division of focal plane sensors to reconstruct S_0 DoLP, and AoP," *Opt. Exp.*, vol. 27, no. 6, pp. 8566–8577, 2019.
- [24] G. C. Sargent, B. M. Ratliff, and V. K. Asari, "Conditional generative adversarial network demosaicking strategy for division of focal plane polarimeters," *Opt. Exp.*, vol. 28, no. 25, pp. 38419–38443, 2020.
- [25] S. Qiu, Q. Fu, C. Wang, and W. Heidrich, "Polarization demosaicking for monochrome and color polarization focal plane arrays," in *Proc. Int. Symp. Vis. Modelling, Vis. (VMV)*, 2019, pp. 117–124.
- [26] S. Qiu, Q. Fu, C. Wang, and W. Heidrich, "Linear polarization demosaicking for monochrome and colour polarization focal plane arrays," *Comput. Graph. Forum*, vol. 40, no. 6, pp. 77–89, 2021.
- [27] S. Wen, Y. Zheng, and F. Lu, "A sparse representation based joint demosaicking method for single-chip polarized color sensor," *IEEE Trans. Image Process.*, vol. 30, pp. 4171–4182, 2021.
- [28] S. Wen, Y. Zheng, F. Lu, and Q. Zhao, "Convolutional demosaicking network for joint chromatic and polarimetric imagery," *Opt. Lett.*, vol. 44, no. 22, pp. 5646–5649, 2019.
- [29] D. Kiku, Y. Monno, M. Tanaka, and M. Okutomi, "Beyond color difference: Residual interpolation for color image demosaicking," *IEEE Trans. Image Process.*, vol. 25, no. 3, pp. 1288–1300, Mar. 2016.
- [30] W. Ye and K. Ma, "Color image demosaicking using iterative residual interpolation," *IEEE Trans. Image Process.*, vol. 24, no. 12, pp. 5879–5891, Dec. 2015.
- [31] Y. Kim and J. Jeong, "Four-direction residual interpolation for demosaicking," *IEEE Trans. Circuits Syst. Video Technol.*, vol. 26, no. 5, pp. 881–890, May 2016.
- [32] Y. Monno, D. Kiku, M. Tanaka, and M. Okutomi, "Adaptive residual interpolation for color and multispectral image demosaicking," *Sensors*, vol. 17, no. 12, pp. 2787–1–2787-21, 2017.
- [33] P.-J. Lapray, L. Gendre, A. Foulonneau, and L. Bigué, "Database of polarimetric and multispectral images in the visible and NIR regions," *Proc. SPIE*, vol. 10677, May 2018, Art. no. 1067738.
- [34] M. Morimatsu, Y. Monno, M. Tanaka, and M. Okutomi, "Monochrome and color polarization demosaicking using edge-aware residual interpolation," in *Proc. IEEE Int. Conf. Image Process. (ICIP)*, Oct. 2020, pp. 2571–2575.
- [35] K. He, J. Sun, and X. Tang, "Guided image filtering," *IEEE Trans. Pattern Anal. Mach. Intell.*, vol. 35, no. 6, pp. 1397–1409, Jun. 2013.
- [36] X. Liu, M. Tanaka, and M. Okutomi, "Practical signal-dependent noise parameter estimation from a single noisy image," *IEEE Trans. Image Process.*, vol. 23, no. 10, pp. 4361–4371, Oct. 2014.
- [37] S. Mihoubi, O. Losson, B. Mathon, and L. Macaire, "Multispectral demosaicking using pseudo-panchromatic image," *IEEE Trans. Comput. Imag.*, vol. 3, no. 4, pp. 982–995, Dec. 2017.

Miki Morimatsu received the B.E. and M.E. degrees from the Tokyo Institute of Technology, Tokyo, Japan, in 2019 and 2021, respectively. Her research interests at the Tokyo Institute of Technology are polarization imaging and image demosaicking.

Yusuke Monno (Member, IEEE) received the B.E., M.E., and Ph.D. degrees from the Tokyo Institute of Technology, Tokyo, Japan, in 2010, 2011, and 2014, respectively. From November 2013 to March 2014, he joined the Image and Visual Representation Group, École Polytechnique Fédérale de Lausanne, as a Research Internship Student. He is currently an Assistant Professor with the Department of Systems and Control Engineering, School of Engineering, Tokyo Institute of Technology. His research interests are in both theoretical and practical aspects of image processing, computer vision, and biomedical engineering.

Masayuki Tanaka (Member, IEEE) received the bachelor's and master's degrees in control engineering and the Ph.D. degree from the Tokyo Institute of Technology in 1998, 2000, and 2003, respectively. He was a Software Engineer at Agilent Technology from 2003 to 2004. He was a Research Scientist with the Tokyo Institute of Technology from 2004 to 2008. He was an Associate Professor with the Graduate School of Science and Engineering, Tokyo Institute of Technology, from 2008 to 2016. He was a Visiting Scholar with the Department of Psychology, Stanford University, from 2013 to 2014. He was an Associate Professor with the School of Engineering, Tokyo Institute of Technology, from 2016 to 2017. He was a Senior Researcher with the National Institute of Advanced Industrial Science and Technology from 2017 to 2020. Since 2020, he has been an Associate Professor with the School of Engineering, Tokyo Institute of Technology.

Masatoshi Okutomi (Member, IEEE) received the B.Eng. degree from the Department of Mathematical Engineering and Information Physics, The University of Tokyo, Tokyo, Japan, in 1981, the M.Eng. degree from the Department of Control Engineering, Tokyo Institute of Technology, Tokyo, in 1983, and the Dr.Eng. degree from the Tokyo Institute of Technology in 1993, for his research on stereo vision. He joined the Canon Research Center, Canon Inc., Tokyo, in 1983. From 1987 to 1990, he was a Visiting Research Scientist with the School of Computer Science, Carnegie Mellon University, Pittsburgh, PA, USA. Since 1994, he has been with the Tokyo Institute of Technology, where he is currently a Professor with the Department of Systems and Control Engineering, School of Engineering.